Featured in Physics

Universal Gate Operations on Nuclear Spin Qubits in an Optical Tweezer Array of ^{171}Yb Atoms

Shuo Ma,[1,2,*] Alex P. Burgers,[1,*] Genyue Liu,[1] Jack Wilson,[1] Bichen Zhang,[1] and Jeff D. Thompson[1,†]

[1]*Princeton University, Department of Electrical and Computer Engineering, Princeton, New Jersey 08544, USA*

[2]*Princeton University, Department of Physics, Princeton, New Jersey 08544, USA*

(Received 13 December 2021; accepted 6 April 2022; published 3 May 2022)

Neutral atom arrays are a rapidly developing platform for quantum science. Recently, alkaline earth atoms (AEAs) have attracted interest because their unique level structure provides several opportunities for improved performance. In this work, we present the first demonstration of a universal set of quantum gate operations on a nuclear spin qubit in an AEA, using ^{171}Yb. We implement narrow-line cooling and imaging using a newly discovered magic trapping wavelength at $\lambda = 486.78$ nm. We also demonstrate nuclear spin initialization, readout, and single-qubit gates and observe long coherence times [$T_1 \approx 20$ s and $T_2^* = 1.24(5)$ s] and a single-qubit operation fidelity $\mathcal{F}_{1Q} = 0.99959(6)$. We also demonstrate two-qubit entangling gates using the Rydberg blockade, as well as coherent control of these gate operations using light shifts on the Yb^+ ion core transition at 369 nm. These results are a significant step toward highly coherent quantum gates in AEA tweezer arrays.

DOI: 10.1103/PhysRevX.12.021028

Subject Areas: Atomic and Molecular Physics
Quantum Information

I. INTRODUCTION

Neutral atom arrays with Rydberg-mediated entanglement are a versatile and rapidly developing tool for quantum computing and simulation [1,2]. In recent years, this approach has been used to study quantum phase transitions [3,4] and probe novel phases of matter [5] in large, two-dimensional systems. At the same time, the performance of quantum gate operations is also improving rapidly [6,7], allowing the generation of many-qubit entanglement [8] and new approaches to quantum state tomography and benchmarking [9].

An emerging frontier within neutral atom arrays is the use of alkaline-earth-like atoms (AEAs) such as Sr [10–12] and Yb [13]. The rich internal structure of these atoms affords numerous unique capabilities, including ground-state Doppler cooling [10,11], trapping of Rydberg states [14], high-fidelity single-photon Rydberg excitation [15], and efficient local control of gate operations using light shifts on the ion core [16,17]. Furthermore, the presence of optical clock transitions opens new applications to frequency metrology [18,19], particularly using entangled states [20].

Another unique capability of fermionic AEA isotopes (with odd masses) is encoding qubits in the nuclear spin of the $J = 0$ electronic ground state. Because of the absence of hyperfine coupling, this qubit should be highly immune to many sources of technical noise, including differential light shifts [21] and Raman scattering [22], while still allowing high-fidelity operations using hyperfine coupling in electronic excited states. Nuclear spin qubits have been experimentally demonstrated in ^{87}Sr tweezer arrays ($I = 9/2$) [12] and in single ^{171}Yb atoms ($I = 1/2$) trapped in an optical cavity [23]. However, a universal set of quantum logic operations, including two-qubit gates through a Rydberg state, has not been demonstrated for nuclear spin qubits in AEAs.

In this work, we present the first such demonstration, using qubits encoded in the nuclear spin of ^{171}Yb. We present high-fidelity imaging of ^{171}Yb atoms in a 30-site optical tweezer array using a newly discovered magic wavelength, as well as techniques for initialization, readout, and one- and two-qubit gate operations. Crucially, the qubit coherence time $T_2^* = 1.24(5)$ s exceeds most recent measurements of hyperfine state coherence times in alkali atom tweezer arrays by 2–3 orders of magnitude [6,7,24,25] because of the dramatically reduced differential light shift from the trap [a notable exception is Ref. [26], where $T_2^* = 0.94(3)$ s for Rb is realized using a circularly

*These authors contributed equally to this work.
†jdthompson@princeton.edu

polarized, magic-intensity trap]. The depolarization time $T_1 = 20(2)$ s (corrected for atom loss) is also significantly improved compared to alkali atoms. These properties enable single-qubit gates with an average fidelity $\mathcal{F}_{1Q} = 0.99959(6)$. We also implement two-qubit gates using the Rydberg blockade, which acts on the nuclear spin through the hyperfine coupling in the Rydberg manifold, and generate Bell pairs with fidelity $\mathcal{F}_B = 0.83(2)$. Lastly, we demonstrate coherent control over the Rydberg gate using light shifts on an optical transition in the Yb^+ ion core. These results provide a foundation for large-scale, high-fidelity quantum logic and simulation using nuclear spin qubits in AEA tweezer arrays, as well as tweezer clocks using fermionic AEA isotopes [27].

II. IMAGING ^{171}Yb ATOMS IN TWEEZERS

High-fidelity imaging of atoms in optical tweezers requires bright fluorescence and efficient cooling. The narrow $^1S_0 \rightarrow {}^3P_1$ transition ($\Gamma = 2\pi \times 182$ kHz, $\lambda = 556$ nm) provides a good balance of high scattering rate and low Doppler temperature and was recently used to image ^{174}Yb atoms in an array of optical tweezers. Imaging with a narrow linewidth benefits from a state-insensitive trap at a magic wavelength, which is achieved at $\lambda = 532$ nm for the π-polarized imaging transition in ^{174}Yb [13,28]. However, this wavelength is no longer magic in ^{171}Yb because of the interplay of the tensor light shift and the hyperfine structure. As a result, we observe poor imaging performance in ^{171}Yb with this trapping wavelength.

To overcome this challenge, we search for a new magic wavelength for this transition in ^{171}Yb. Using literature dipole matrix elements [29] and measurements in ^{174}Yb tweezer arrays at various wavelengths, we predict that a magic wavelength for ^{171}Yb transition should occur near 486 nm (see Appendix B). We verify this prediction using a direct measurement with ^{171}Yb atoms. In an optical tweezer array at $\lambda = 486.78$ nm (in vacuum), we find a light shift of $0.0001(6)U_0$ for the $F' = 3/2$ $|m_{F'}| = 1/2$ transitions, compared to $0.3U_0$ for the $|m_{F'}| = 3/2$ transitions, where U_0 is the ground-state trap depth. From this measurement at a single wavelength, we estimate that the exact magic wavelength is in the range $\lambda = 486.78 \pm 0.1$ nm.

At this wavelength, we obtain imaging and cooling performance comparable to ^{174}Yb. In a 30-site array using a power of 5 mW per tweezer, we perform repeated imaging of single atoms with a combined fidelity and survival probability between images of 98.8(3)% [Fig. 1(c)], using an exposure time of 25 ms. The atomic temperature during imaging is $T = 27$ μK. The fidelity is dominated by atom loss during imaging, which arises from Raman scattering into the metastable states $^3P_0$ and $^3P_2$ [13], and could be improved by repumping these states.

We also observe vanishing light shifts for the $^3P_1$ $|m_{F'}| = 1/2$ transition in an optical tweezer at the clock magic wavelength transition of 759.35 nm [30], which is promising for future experiments on tweezer clocks [18,19] using $I = 1/2$ hyperfine isotopes [27].

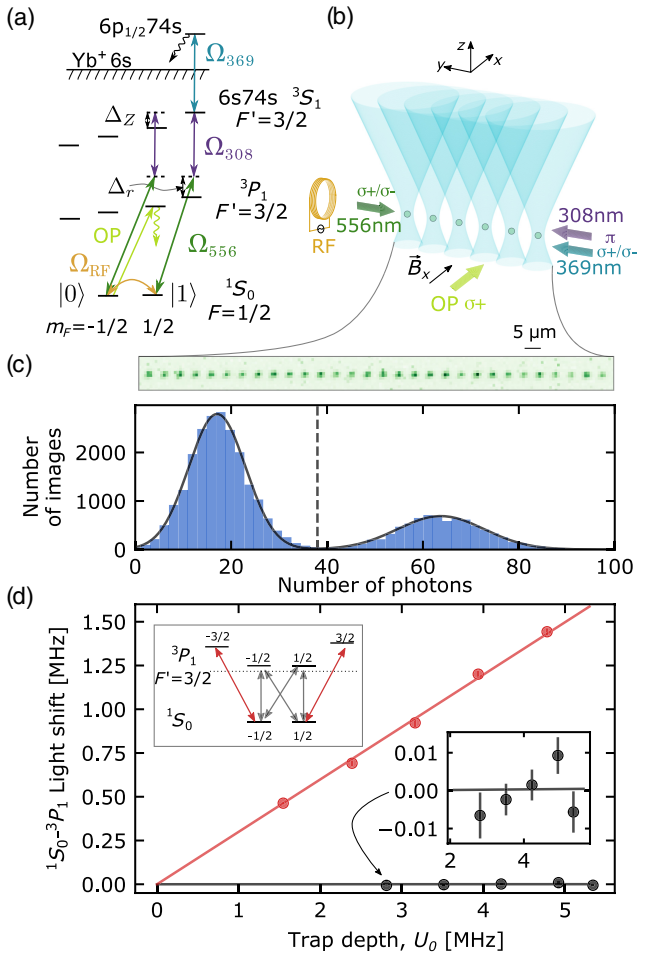

FIG. 1. (a) ^{171}Yb level diagram. A qubit is encoded in the nuclear spin sublevels of the $^1S_0$ ground state and initialized into $|1\rangle$ via optical pumping (OP). Spin rotations are performed using an rf field. Two-qubit gates are performed using the $6s74s$ $^3S_1$ $|F, m_F\rangle = |3/2, 3/2\rangle$ level, accessed via two-photon excitation through $^3P_1$. State readout is performed by blowing out atoms in $|1\rangle$ by autoionization from the Rydberg state. (b) Orientation of the control fields and tweezers. (c) Histogram of photons detected in a single tweezer region during a 25 ms image, and a fluorescence image of a 30-site array averaged over 1000 single-shot images without rearrangement. (d) Differential light shift measurement on the ^{171}Yb $^1S_0$-$^3P_1$ transition in tweezers with $\lambda = 486.78$ nm. The $F' = 3/2$ manifold is split by the tensor light shift, giving a differential shift of $0.3U_0$ for $|m_{F'}| = 3/2$ and $0.0001(6)U_0$ for $|m_{F'}| = 1/2$. The error bar corresponds to one standard deviation uncertainty in the fitted resonant frequency.

III. SINGLE-QUBIT OPERATIONS

We encode qubits in the sublevels of the $F = 1/2$ $^1S_0$ level and label the states $|m_F = -1/2\rangle \equiv |0\rangle$ and

$|m_F = 1/2\rangle \equiv |1\rangle$ [Fig. 1(a)]. Since there is no hyperfine coupling in $^1S_0$, initialization and readout rely on the hyperfine and Zeeman shifts of the excited states [Fig. 1(a)]. State initialization is performed using optical pumping (OP) with σ^+-polarized light, on the $|0\rangle \rightarrow |^3P_1, F' = 3/2, m_{F'} = 1/2\rangle$ transition. A magnetic field ($B_x = 4.11$ G) shifts the $m_{F'} = 3/2$ transition by 5.7 MHz $= 31\Gamma/(2\pi)$, ensuring that $|1\rangle$ is a dark state.

Spin readout is performed by selectively blowing out atoms in $|1\rangle$, via autoionization from the Rydberg state. We use the $^3S_1$ $6s74s$ Rydberg state $|F' = 3/2, m_{F'} = 3/2\rangle$, which has not been previously observed, to the best of our knowledge (Appendix C). We excite this state in a two-photon process through $^3P_1$, with intermediate state detuning $\Delta_r = 2\pi \times 20$ MHz. The two-photon Rabi frequency is $\Omega_r = 2\pi \times 0.31$ MHz. Excitation of $|0\rangle$ is prevented by a Zeeman splitting in the Rydberg manifold, $\Delta_Z = 2\pi \times 7.8$ MHz $\gg \Omega_r$. Following a π pulse on this transition, any Rydberg atoms are rapidly autoionized by exciting the $6s \rightarrow 6p_{1/2}$ (369 nm) Yb^+ ion core transition [15,16,31], and atoms remaining in $|0\rangle$ are detected via fluorescence imaging. The tweezers are turned off for 5 μs during the Rydberg excitation and autoionization steps to avoid inhomogeneous light shifts.

We characterize the detection protocol by performing N_r blowout cycles before imaging [Fig. 2(a)]. Because of imperfect Rydberg π pulses, some atoms in $|1\rangle$ remain after a single round, but this population is suppressed exponentially with additional rounds. With $N_r = 3$, we detect a surviving atom with probability of 94.5(3)% [0.2(2)%] after preparation in $|0\rangle$ ($|1\rangle$), corresponding to a raw average initialization and readout fidelity of 97.2(4)%, and a probability to initialize the atom in the wrong spin state of less than 0.2(2)%. In the case that we intend to prepare and measure the atom in $|0\rangle$ (bright state), we can attribute most of the observed error to imperfect atom loading [i.e., the atom does not survive the initial image, 1.2(3)%], as well as atom loss (1%) and Raman scattering to $|1\rangle$ [1.2(2)%] during the spin readout. These effects do not give rise to significant errors for preparation and detection in $|1\rangle$ (dark state), which is why the correct outcome is observed more often after initializing in $|1\rangle$.

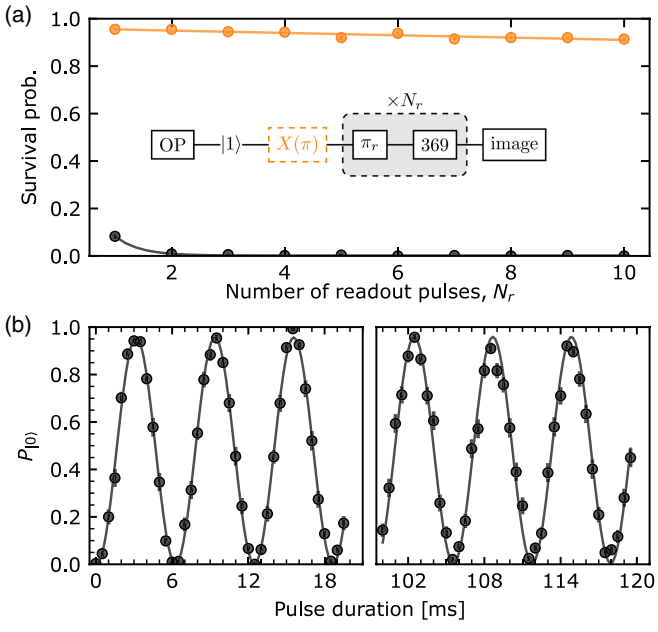

FIG. 2. (a) Atom survival probability after N_r repetitions of the blowout sequence through the Rydberg state, after preparing an atom in $|1\rangle$ (black) and $|0\rangle$ (orange). (b) Rabi oscillations of the nuclear spin qubit, with $\Omega_{\rm rf} = 2\pi \times 161.7(5)$ Hz. The error bars indicate the statistical uncertainty ($\pm 1\sigma$) in the measured survival probability.

Next, we demonstrate coherent manipulation of the nuclear spin qubit. The magnetic field splits the nuclear spin hyperfine levels by 750 Hz/G, resulting in a Larmor frequency $\omega_L \approx 2\pi \times 3.09$ kHz. This enables qubit rotations using an rf (radio frequency) coil. We observe long-lived nuclear spin Rabi oscillations with Rabi frequency $\Omega_{\rm rf} = 2\pi \times 161.7(5)$ Hz [Fig. 2(b)]. The small value of $\Omega_{\rm rf}$ is chosen to avoid counterrotating terms when $\Omega_{\rm rf} \approx \omega_L$. Faster rotations are readily accessible with larger static fields or by implementing a second coil to generate σ^+-polarized rf.

To quantify the qubit coherence, we perform a Ramsey measurement, including a synthetic detuning to map the coherence onto population oscillations [Fig. 3(a)]. Fitting the data from each site individually yields an average $T_2^* = 1.24(5)$ s. Averaging the populations across the array before fitting [Fig. 3(a)] results in a slightly lower value $\bar{T}_2^* = 1.00(4)$ s because of a magnetic field gradient giving a shift of approximately 2 mHz/μm in the array direction.

To mitigate slowly varying noise and inhomogeneity, we perform a spin-echo measurement. At each hold time, we vary the phase of the second $\pi/2$ pulse and extract the coherence from the visibility of the resulting oscillation [Fig. 3(b)], removing the effect of magnetic field gradients and shot-to-shot fluctuations. The raw visibility decays to $1/e$ after 3.9(3) s. Normalizing to the mean survival probability to remove the effect of atom loss gives an estimate of the intrinsic $1/e$ decoherence time of $T_2 = 5(1)$ s. We attribute this residual decoherence to magnetic field drifts during each experiment, arising from thermal effects in our current source. These drifts also result in a slight chirp in the Ramsey fringes of 1.97 Hz/s, determined from a fit to the data in Fig. 3(a).

We also measure the depolarization time T_1 after initializing in each spin state [Fig. 3(c)]. Atom loss occurs on a timescale $T_a = 9$ s. By normalizing the spin state population to the fraction of atoms remaining, we extract the intrinsic spin flip rates starting from each state: $T_1^{|0\rangle} = 13(2)$ s and $T_1^{|1\rangle} = 27(2)$ s. In the absence of hyperfine coupling in $^1S_0$, the predicted Raman scattering rate is extremely small, of the order of 10^{-13} s^{-1} [22], and we

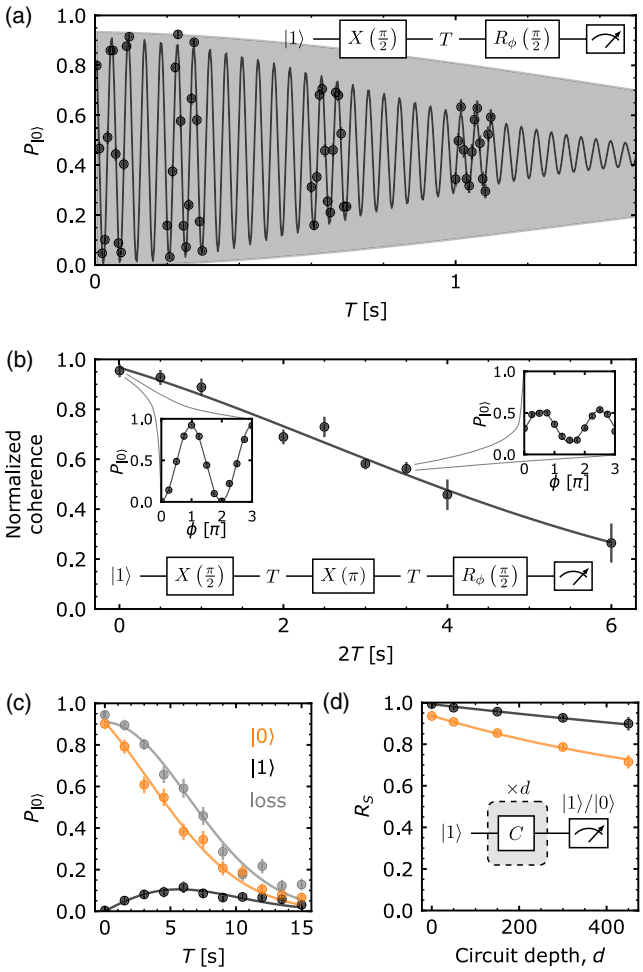

FIG. 3. Coherence measurements of the ^{171}Yb nuclear spin qubit. (a) Array-averaged Ramsey fringes with fitted $1/e$ decay time of $\bar{T}_2^* = 1.00(4)$ s [fitting sites individually yields an average $T_2^* = 1.24(5)$ s]. The gray shaded envelope indicates the contribution from a magnetic field gradient across the array. (b) Spin-echo measurement. The phase of the final $\pi/2$ pulse is scanned for each wait time T, and the coherence is extracted from the visibility (insets) and normalized to the mean survival. The normalized coherence decays to $1/e$ after a time $T_2 = 5(1)$ s. (c) Spin T_1 measurement. The orange (black) points show the probability to detect an atom in $|0\rangle$ following initialization in $|0\rangle$ ($|1\rangle$). The gray points show survival probability without the spin readout sequence (i.e., atom loss), which decays to $1/e$ after $T_a = 9.0(3)$ s. Using survival-normalized populations, we infer an intrinsic $1/e$ spin flip time for each state: $T_1^{|0\rangle} = 13(2)$ s and $T_1^{|1\rangle} = 27(2)$ s. (d) Randomized benchmarking of single-qubit rotations. Orange (black) points show the probability to obtain the correct result for sequences ending in $|0\rangle$ ($|1\rangle$). From the decay rates, we obtain an average gate fidelity of 99.959(6)%. In all panels, the error bars show $\pm 1\sigma$ statistical error.

attribute the observed spin flip rate to leaked resonant light from a beam path without a mechanical shutter.

Lastly, we study the single-qubit gate fidelity with randomized benchmarking (RB). We use pyGSTi [32] to generate random sequences of Clifford group operations of varying depth (40 sequences per depth). The ideal output of the RB circuit is chosen to be $|0\rangle$ or $|1\rangle$ with equal probability. The probability to get the correct output, R_S, is measured and fitted [Fig. 3(d)] to extract the average operation fidelity according to

$$R_S = \frac{1}{2} + \frac{1}{2}(1 - 2\epsilon_{\text{spam}})(1 - 2\epsilon_{\text{gate}})^d, \tag{1}$$

where ϵ_{spam} is the state preparation and measurement error, ϵ_{gate} is the average gate error, and d is the circuit depth. We find the average gate fidelity $\mathcal{F}_{1Q} = 1 - \epsilon_{\text{gate}}$ to be 99.975(1)% and 99.927(3)% using RB circuits with an ideal output state in $|1\rangle$ and $|0\rangle$, respectively, for an average fidelity of 99.959(6)%. The difference in fidelity between the two output states is consistent with atom loss, given the sequence duration of $d \times 4$ ms. The average $\epsilon_{\text{spam}} = 0.025(6)$.

IV. TWO-QUBIT ENTANGLING GATE

To complete the universal set of operations, we implement a two-qubit gate based on the Rydberg blockade [33]. A number of blockade-based gate protocols have been demonstrated [6,7,34–36], based on selective coupling of one of the qubit levels to a Rydberg state. In our work, we realize selective coupling of $|1\rangle$ to the Rydberg state by applying a magnetic field that produces a large Zeeman shift $\Delta_z \gg \Omega_r$ in the Rydberg state [Sec. III, Fig. 1(a)]. In this arrangement, the nuclear spin is manipulated using the hyperfine coupling in the $F' = 3/2$ Rydberg state. For the two-qubit gate protocol, we use a larger Rabi frequency $\Omega_r = 2\pi \times 0.763$ MHz ($\Delta_Z/\Omega_r = 10.6$).

We implement the controlled-Z (CZ) gate protocol of Ref. [7], because it acts symmetrically on the atoms and does not require local addressing of the Rydberg excitation light. The gate consists of two pulses of length τ, detuning Δ, and Rabi frequency Ω_r, but with a phase slip ξ on the second pulse [Fig. 4(b)]. The behavior can be understood by considering the evolution of the computational basis states. The state $|00\rangle$ does not undergo any dynamics. The state $|01\rangle$ ($|10\rangle$) undergoes detuned Rabi oscillations to $|0r\rangle$ ($|r0\rangle$). The state $|11\rangle$ undergoes detuned Rabi oscillations to $|W\rangle = (|1r\rangle + |r1\rangle)/\sqrt{2}$, with a Rabi frequency of $\sqrt{2}\Omega_r$, since the Rydberg blockade suppresses excitation to $|rr\rangle$. The difference in Rabi frequencies allows the pulse detuning and duration to be chosen to return both $|01\rangle$ and $|11\rangle$ to themselves at the end of the gate [Fig. 4(c)], but with distinct phase accumulations:

$$\begin{aligned}
|00\rangle &\rightarrow |00\rangle, \\
|01\rangle &\rightarrow |01\rangle e^{i\phi_{01}}, \\
|10\rangle &\rightarrow |10\rangle e^{i\phi_{10}}, \\
|11\rangle &\rightarrow |11\rangle e^{i\phi_{11}}.
\end{aligned}$$

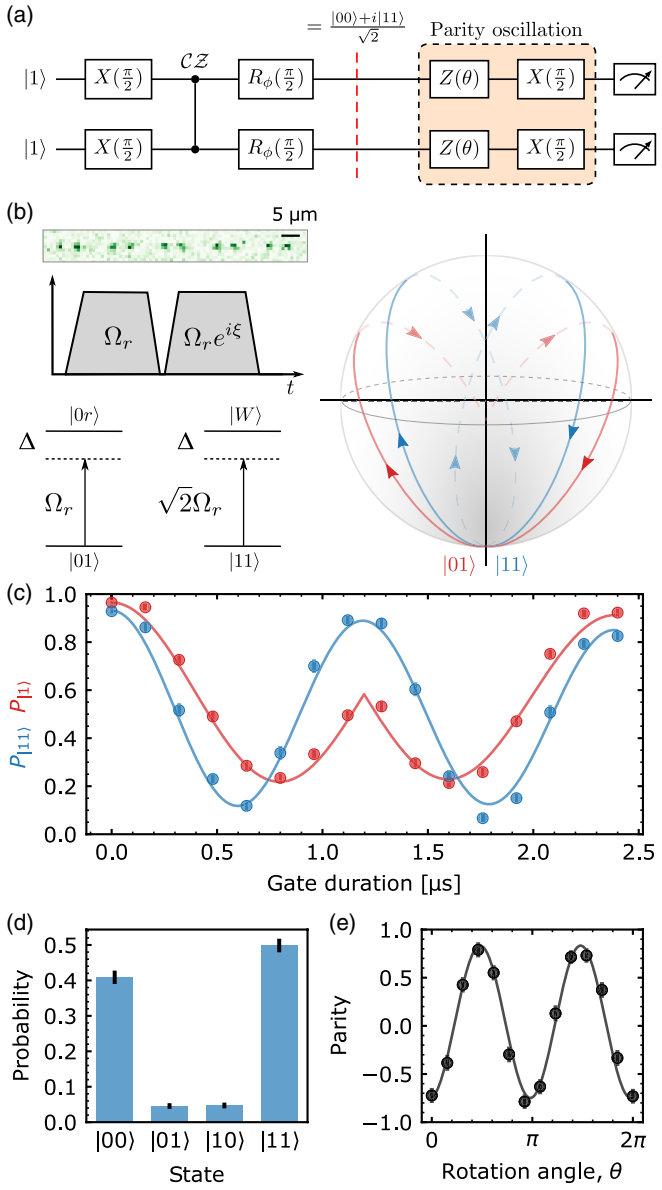

FIG. 4. Two-qubit gate. (a) Circuit diagram of the two-qubit gate characterization experiment. (b) Single-shot image of atom pairs created using rearrangement. The gate consists of two Rydberg pulses, with a phase shift on the second pulse. The level diagrams and Bloch sphere trajectories indicate the dynamics for the computational states $|01\rangle$ (red) and $|11\rangle$ (blue). (c) Evolution of the states $|1\rangle$ (blue, used as a proxy for $|01\rangle$) and $|11\rangle$ (red) state during the gate. The solid lines are simulations using the master equation with a phenomenological dephasing contribution. (d) Measured state populations at the circuit location indicated by the red dashed line. (e) Parity oscillations, with contrast $\mathcal{C} = 0.79(3)$. In all panels, the error bars show $\pm 1\sigma$ statistical error.

For $\Delta/\Omega_r \approx 0.377$, $\xi \approx 3.902$, and $\tau\Omega_r \approx 4.293$, $\phi_{11} = 2\phi_{01} + \pi$, realizing a CZ gate [7].

We experimentally implement the CZ gate in parallel on five pairs of atoms in a dimerized array, generated deterministically using rearrangement. The atomic separation within a dimer is 2.4 μm, considerably less than the measured blockade radius of 14(1.4) μm (see Appendix C), while the spacing between dimers is 31.2 μm. The state dynamics during the gate are depicted schematically in Fig. 4(b) and measured in Fig. 4(c).

To determine the fidelity of the complete gate, we use the circuit in Fig. 4(a). We prepare the two-atom state $[(|0\rangle - i|1\rangle)/\sqrt{2}]^{\otimes 2}$, apply the CZ gate, and then drive a $\pi/2$ pulse to produce the Bell state $|\phi\rangle = (|00\rangle + i|11\rangle)/\sqrt{2}$. The rotation axis of the second pulse is at an angle $\phi = -6.6$ rad with respect to the initial pulse, to compensate the single-qubit phase ϕ_{01} and a light shift from the 556 nm beam. The fidelity is determined from the state populations [Fig. 4(d)] and the contrast $\mathcal{C}$ of parity oscillations [Fig. 4(e)] following an additional single-qubit rotation, according to Ref. [37]:

$$\mathcal{F}_B = \frac{1}{2}(p_{00} + p_{11} + \mathcal{C}), \tag{2}$$

where p_{00} and p_{11} are the populations in $|00\rangle$ and $|11\rangle$, respectively.

We obtain a raw Bell state fidelity of $\mathcal{F}_B = 85(2)\%$. This value is affected by errors in the state preparation and measurement (SPAM), as well as leakage to the Rydberg state. Correcting for these effects with independent measurements, we determine a conservative lower bound on the Bell state fidelity: $\mathcal{F}_B^c \geq 83(2)\%$ (Appendix D). This is limited by several factors, including spontaneous emission from the intermediate and Rydberg states (approximately 3%), as well as laser noise and Doppler decoherence, which are more problematic for the relatively small value of Ω_r used here [38]. This gate fidelity is consistent with a master equation simulation including a phenomenological ground-Rydberg dephasing time of 3.5 μs, which matches an experimental measurement of the same quantity using similar experimental parameters.

V. CONTROLLING THE TWO-QUBIT GATE

Lastly, we demonstrate coherent control of the two-qubit gate operation using a light shift on $|r\rangle$ arising from the Yb^+ ion core transition ($\lambda = 369$ nm), which is driven by a (global) control field [16]. By shifting the $|1\rangle \rightarrow |r\rangle$ transition out of resonance with the Rydberg excitation beam during the CZ gate [Fig. 5(a)], the action of the gate is suppressed [Fig. 5(b)]. In this experiment, the control field intensity is approximately 700 W/cm^2, and it is detuned by $\Delta_c = -2\pi \times 5$ GHz from the $6s74s \rightarrow 6p_{1/2}74s$ (autoionization) transition. We measure a light shift of $-18.3(1)$ MHz on $|r\rangle$. This intensity and detuning match the values used during the spin-selective blowout.

We quantify the coherence of this approach to gate control in two ways. First, we implement the circuit in Fig. 5(a), where the suppressed CZ gate should result in the identity operation (plus a single-qubit phase, compensated

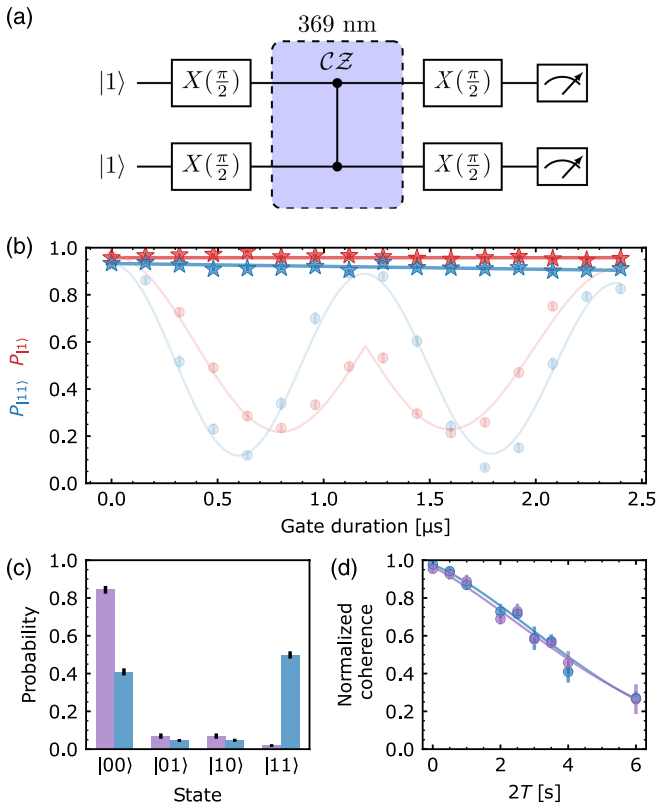

FIG. 5. Coherent control of a Rydberg gate using an ion core light shift. (a) The two-qubit gate is suppressed by applying light near resonance with a Yb^+ ion core transition (369 nm) during the gate. (b) Evolution of the states $|1\rangle$ (red stars) and $|11\rangle$ (blue stars) during a suppressed gate. The dynamics without the control light are shown for comparison [reproduced from Fig. 4(c)]. (c) Measured state populations with (purple) and without (blue) the control light. (d) Coherence of the nuclear spin in $^1S_0$ under continuous illumination with the control light (purple). The measured $T_2 = 5.1(7)$ s is consistent with Fig. 3(b) (reproduced here, in blue). In all panels, the error bars show $\pm 1\sigma$ statistical error.

by the second single-qubit pulse). The ideal circuit output is then $|00\rangle$, and we can quantify the state fidelity by measurement in the population basis [Fig. 5(c)]. We obtain a raw fidelity of $\mathcal{F}_I = 84(2)\%$, or $\mathcal{F}_I^c = 93(3)\%$ after SPAM correction (Appendix D). We attribute the infidelity to Raman scattering [4(2)%] from the 556 nm gate beam and autoionization from a small Rydberg population that is present despite the control beam [2(1)%]. The former can be suppressed using single-photon excitation (i.e., starting in $^3P_0$), while the latter can be suppressed by higher control beam power or detuning [16].

Second, we directly measure the qubit decoherence and depolarization induced by the control beam. We perform Ramsey, spin-echo, and T_1 measurements with continuous illumination from the control beam and find zero effect in all cases [e.g., Fig. 5(d)]. We also measure the differential light shift on qubit levels resulting from the control beam and obtain a value of 40(14) mHz, approximately 10^{-9} times smaller than the light shift of the Rydberg state under the same conditions. This indicates that the control beam has minimal perturbation on the ground-state qubits.

VI. DISCUSSION

The long coherence times observed in this work are important not only for improved gate fidelity, but also for taking advantage of other aspects of the optical tweezer architecture, such as preserving qubit coherence while moving atoms [24,39]. In alkali atoms in optical tweezers, T_2^* is often limited to 1–2 ms by fractional differences in the trap potentials for the qubit states of the order of $\eta \approx 10^{-3}$ [6,24,25,40] [a notable exception is Ref. [26], using hyperpolarizability to realize magic intensity traps with $\eta = 0$, and $T_2^* = 0.94(3)$ s]. For nuclear spin qubits, we expect $\eta = 0$ for linearly polarized light and experimentally measure $\eta = 9.8 \times 10^{-8}$. This limits T_2^* to 15 s, implying another origin for the observed decoherence, such as magnetic field instabilities. Alkali atoms in tweezers also experience Raman scattering that leads to depolarization on a timescale $T_1 \approx 0.5$–1 s [6,25,40]. In ^{171}Yb, this should be very strongly suppressed by the absence of hyperfine coupling in $^1S_0$ [22]. We believe that the observed value $T_1 \approx 20$ s is limited by resonant light leakage. We note that longer coherence times and T_1 times have been observed in ^{87}Sr in tweezers, suggesting room for improvement in ^{171}Yb [12].

Second, we note that a promising direction for future work is to store qubits in the metastable $^3P_0$ state, which has a spontaneous emission-limited lifetime of $\tau = 20$ s. This preserves the benefits of the nuclear spin qubit in $^1S_0$ but also enables single-photon Rydberg excitation ($\lambda = 302$ nm). Single-photon gates can be much faster, resulting in reduced sensitivity to Doppler shifts and laser phase noise [38,41], and also do not experience intermediate state scattering. Using single-photon Rydberg excitation from $^3P_0$, ground-Rydberg Bell states with a fidelity greater than 99% have been recently demonstrated in ^{88}Sr [15], and this should translate directly to nuclear spin gates in the $^3P_0$ state of ^{171}Yb.

Third, we note that this work demonstrates the first observation of the $^3S_1$ Rydberg series in ^{171}Yb and, to the best of our knowledge, the first measurement of the Rydberg blockade in a hyperfine isotope of any AEA. While the Rydberg blockade for Yb $^1S_0$ series in ^{174}Yb was predicted to be very small [42], there have been no predictions of the $^3S_1$ blockade strength in ^{174}Yb or ^{171}Yb. We recently demonstrated that the $^3S_1$ series in ^{174}Yb has a strong blockade [14,16], and, in this work, we have extended these results to ^{171}Yb. The observed blockade strength has significant uncertainty (Appendix C) but appears to be larger than the blockade in the alkali atoms Rb or Cs at the same n, which may be the result of a

hyperfine-induced Förster resonance [43]. Confirming this result requires further spectroscopic measurements, particularly of the ^3P_J Rydberg states.

Lastly, while all of the demonstrated gate operations in this work are global, the extension to local operations is straightforward. Local single-qubit operations can be implemented using degenerate Raman transitions, while local two-qubit operations can be implemented by locally addressing one or both beams involved in the Rydberg excitation or by locally addressing the 369 nm control beam to create local light shifts on $|r\rangle$ [16]. The latter approach benefits from less required addressing power for high-fidelity gates [16] and is also significantly insensitive to variations in the local intensity, as the differential light shift is negligible. It can also be used to control single-photon Rydberg excitation (e.g., gates on nuclear spin qubits in $^3P_0$).

VII. CONCLUSION

In this work, we have demonstrated the first universal set of quantum gate operations for nuclear spin qubits in AEA tweezer arrays, using ^{171}Yb. In particular, we implemented imaging, initialization, readout, one- and two-qubit gate operations, and coherent control of Rydberg excitation using a light shift on an ion core transition. In recent work, AEAs in optical tweezers have also been used to demonstrate extremely high-fidelity atom detection [44], highly coherent clock state manipulation [18], record Rydberg entanglement fidelities [15], and efficient light shifting techniques and state detection using the ion core [15,16,31]. Combining these techniques with nuclear spin qubits is a very promising avenue for realizing scalable, high-fidelity quantum gate operations, as well as entanglement-enhanced tweezer clocks using fermionic isotopes [45,46].

ACKNOWLEDGMENTS

We gratefully acknowledge Sam Saskin, for contributions to the experiment and developing an understanding of ^{171}Yb Rydberg states, and Francesco Scazza, for assistance with preliminary measurements of magic trapping wavelengths. This work was supported by ARO (W911NF-18-10215), ONR (N00014-20-1-2426), DARPA ONISQ (W911NF-20-10021), and the Sloan Foundation.

Note added.—Recently, we became aware of complementary work demonstrating ^{171}Yb qubits in tweezer arrays [47].

APPENDIX A: EXPERIMENTAL APPARATUS

A hot Yb atomic beam from an oven is cooled in a 2D magneto-optical trap (MOT) on the $^1S_0 \rightarrow {}^1P_1$ transition ($\Gamma = 2\pi \times 31$ MHz, $\lambda = 399$ nm). Cold atoms are pushed into a science chamber glass cell and loaded into a 3D MOT on the $^3P_1$ transition. Using the MOT, we measure a vacuum limited lifetime of approximately 30 s. Atoms are loaded from the MOT into tweezers with $\lambda = 486.78$ nm (Coherent Genesis MX). The array is generated using a crossed pair of acousto-optic deflectors (AODs) controlled using an arbitrary waveform generator (AWG) from Spectrum Instrumentation (M4i.6622-x8) and projected through a 0.6 NA objective (Special Optics). Atoms are imaged using a single, retroreflected beam with a projection onto all three trap axes. The $1/e$ lifetime for atoms in the tweezers is approximately 9 s, which we attribute to heating from intensity noise in the trap laser. We do not apply any repumping light to depopulate the $^3P_{0,2}$ states. A detailed description of the apparatus can be found in Ref. [13].

The Rydberg laser system consists of two sources: 556 (green, $^1S_0 \rightarrow {}^3P_1$) and 308 nm (UV, $^3P_1 \rightarrow 6s74s\,{}^3S_1$ $F' = 3/2, m_{F'} = 3/2$) light. The green excitation light is generated via sum frequency generation in a periodically poled lithium niobate crystal, using an amplified erbium fiber laser (1565 nm) and a titanium-sapphire (TiS) laser at 862 nm (M Squared Solstis). To produce UV light, we first generate 616 nm (orange) light using the same process described above and then double it in a resonant cavity (LEOS Rondo). The green and orange light frequencies are stabilized on a ultra-low expansion reference cavity.

The green (σ^+/σ^--polarized) and UV (π-polarized) beams are counterpropagating and focused to 30 and 15 μm $1/e^2$ radius at the atoms, respectively. Typical measured single-photon Rabi frequencies are $\Omega_{\text{green}} = 2\pi \times 5.5$ MHz and $\Omega_{\text{UV}} = 2\pi \times 5.5$ MHz. The latter value is obtained with a UV power of approximately $P_{\text{UV}} = 18$ mW. The 369 nm control beam used for autoionization and light shifts is copropagating with the 308 nm Rydberg laser but orthogonally polarized. The position and angle of the UV beam are monitored using cameras to ensure stable alignment to the atoms.

The array spacing is dynamically controlled during the experiments using AODs. During imaging and rearrangement, the atoms are separated by 4.8 μm [Fig. 1(c)]. During the blowout operation [Fig. 2(a)], the spacing is expanded to 31.6 μm, to avoid blockade effects. During the two-qubit gates (Secs. IV and V), the atoms are arranged in pairs. The spacing within a pair is 2.4 μm, ensuring strong Rydberg blockade, while the spacing between pairs is 31.2 μm, ensuring negligible cross-blockade. After the gate, the array is expanded to 31.6 μm spacing for the blowout protocol and then rearranged to the configuration shown in Fig. 4(b) for imaging (4.8 μm separation within a pair and 9.6 μm between pairs).

APPENDIX B: ^{171}Yb MAGIC WAVELENGTH

A trapping wavelength of 532 nm is magic for the $^1S_0$-$^3P_1$ transition in ^{174}Yb, but not in ^{171}Yb, because of the interplay of the tensor light shift and hyperfine coupling. While we are able to image ^{171}Yb atoms in 532 nm traps,

the combined imaging fidelity and survival probability only reaches 94%. Furthermore, achieving this performance requires an imaging duration of 150 ms and a trap depth approximately 4 times deeper than required for ^{174}Yb.

To realize improved imaging performance for ^{171}Yb, we identify a different trapping wavelength that is magic for the $^1S_0$-$^3P_1$ transition in that isotope. To determine this wavelength, we measure the differential light shifts for the π- and σ-polarized transitions in ^{174}Yb: $\Delta U_0 = U_0 - \tilde{U}_0$ and $\Delta U_1 = U_1 - \tilde{U}_0$, respectively (Fig. 6). We report the ratio of these quantities, $\Delta U_0/\Delta U_1$, which is not subject to calibration errors in the absolute intensity. The data are qualitatively reproduced by a model incorporating computed matrix elements [29], with the inclusion of free parameters accounting for state-dependent core polarizability [48].

The magic wavelengths for ^{171}Yb can be computed from the shifts of the ^{174}Yb transitions. A magic wavelength for the transition to the $(F', |m_{F'}|) = (3/2, 3/2)$ excited states occurs when $\Delta U_1 = 0$, while the transition to the $(F', |m_{F'}|) = (3/2, 1/2)$ states is magic when $\Delta U_0/\Delta U_1 = -1/2$. We focus on the latter case, because the dipole orientation provides more favorable fluorescence collection efficiency.

From the data in Fig. 6(b), we predict that such a magic wavelength should occur near 486 nm and near 750 nm. Using direct measurements in ^{171}Yb, we determine a precise value for the short-wavelength magic wavelength [Fig. 1(d)]. We also experimentally confirm that the $^1S_0$-$^3P_0$ clock transition magic wavelength at 759.35 nm [27,30] is also very close to magic for $^1S_0$-$^3P_1$, by measuring the light shift in a single tweezer at this wavelength.

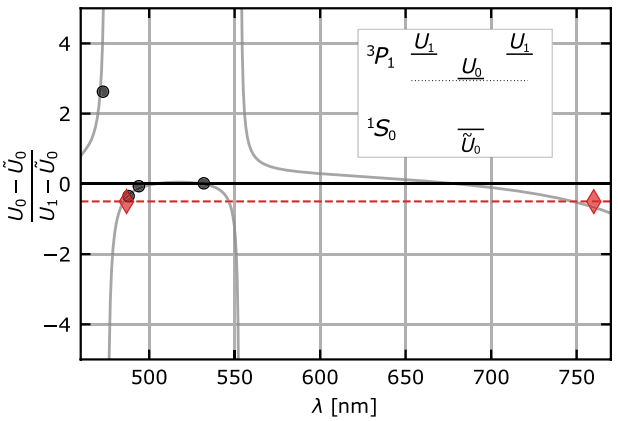

FIG. 6. Ratio of the differential light shifts for the $^1S_0$-$^3P_1$ transition in ^{174}Yb, for the $m_{J'} = 0$ ($\Delta U_0 = U_0 - \tilde{U}_0$) and $|m_{J'}| = 1$ ($\Delta U_1 = U_1 - \tilde{U}_0$) transitions. The black points show measurements from ^{174}Yb, while the red points show inferred values from measurements with ^{171}Yb. A magic wavelength for the ^{171}Yb $^1S_0$-$^3P_1$ $F' = 3/2, |m_{F'}| = 1/2$ transition occurs when $\Delta U_0/\Delta U_1 = -1/2$ (dashed red line), which we confirm in ^{171}Yb at 486.78 nm and near 759 nm. The gray line is an approximate model to guide the eye. Inset: level diagram indicating the light shift on each state in ^{174}Yb.

APPENDIX C: ^{171}Yb RYDBERG STATES

In this work, we use the Rydberg state $6s74s\ ^3S_1$, with $F' = 3/2$. The Yb $^3S_1$ Rydberg series in ^{174}Yb was first observed in Ref. [14], and, to the best of our knowledge, this series has not previously been studied in ^{171}Yb. The Rydberg states of hyperfine isotopes in divalent atoms have a rich structure arising from the large hyperfine coupling in the ion core (12.6 GHz in the case of ^{171}Yb) [49,50]. This gives rise to distinct Rydberg series converging to different ionization limits associated with different hyperfine states in the ion core. The emergence of these series from the LS-coupled states can be understood to arise from singlet-triplet mixing induced by hyperfine coupling [49,50].

In this picture, the $^3S_1$ $F' = 3/2$ series is simple: It does not experience singlet-triplet mixing and converges to the Yb^+ $F = 1$ threshold. We identify this state by its quantum defect relative to this threshold, which is the same as the ^{174}Yb $^3S_1$ series ($\delta = 4.439$), and also by the measured g factor $g_F = 1.35$, consistent with the theoretical value of 4/3. The total excitation energy from $^1S_0$ to $|r\rangle$ is 1511.569 505(60) THz.

However, many of the other Rydberg series in ^{171}Yb have more complex behavior, which makes calculations of the interaction potentials rather challenging [43]. This challenge is compounded by the strongly perturbed ^3P_J series [51].

Therefore, to validate the use of the Rydberg blockade in ^{171}Yb, we experimentally measure the van der Waals interaction for the $6s74s\ ^3S_1$ $|F, m_F\rangle = |3/2, 3/2\rangle$ state (Fig. 7). The measurement is performed by preparing atom pairs with varying spacing, driving the transition to $|r\rangle$ on resonance, and fitting the frequency of the observed Rabi oscillations at each separation. This frequency increases from Ω to $\sqrt{2}\Omega$ when $V > \Omega$.

We find a value for the blockade radius of $R_b = 14(1.4)$ μm when $\Omega = 2\pi \times 0.63$ MHz. This implies a C_6 coefficient of $5(3)$ THz $\cdot\, \mu$m^6. The large uncertainty in this value comes from uncertainty in the magnification of our imaging system. We estimate the magnification from the component specifications, but do not directly measure it, and assign an uncertainty of $\pm 10\%$.

We note the estimated C_6 is large, 3.1 times larger than for S states in Rb at the same n [52]. We also measure C_6 for $n = 50$ in ^{174}Yb using the same technique and apparatus, finding $15(8)$ GHz $\cdot\, \mu$m^6 [16]. Scaling to $n = 74$ by $(n^*)^{11}$ gives a value 2.9 times smaller than the observed ^{171}Yb $n = 74$ value. Both observations are consistent with a smaller Förster energy defect [53] giving rise to an enhanced blockade in ^{171}Yb, and we note that

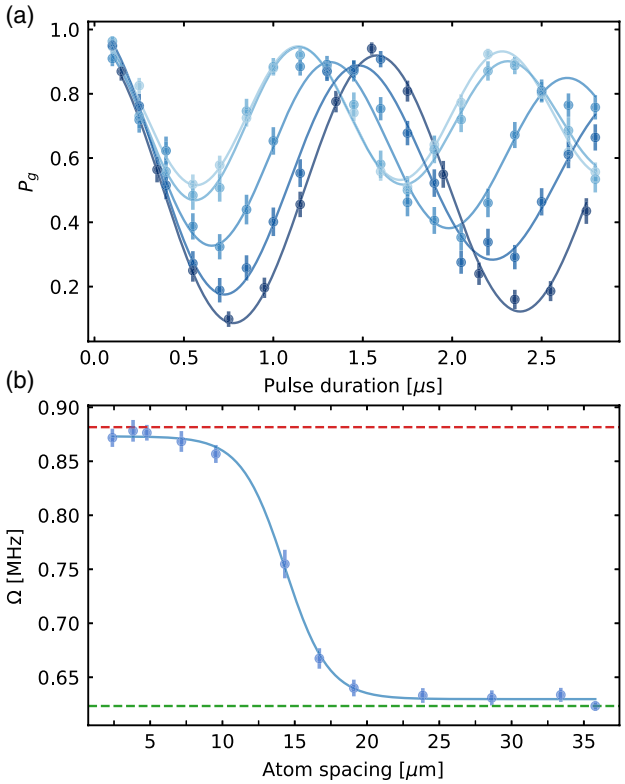

FIG. 7. Measuring the blockade radius. (a) We observe Rabi oscillations dimers with atom separations between 36 (dark blue) and 2.4 μm (light blue). (b) The fitted oscillation frequency as a function of atomic spacing. The oscillation frequency increases from $\Omega_r = 2\pi \times 0.63$ MHz (green dashed line) to approximately $\sqrt{2}\Omega_r$ (red dashed line) in the blockade regime. The deviation from the exact $\sqrt{2}$ ratio is attributed to a drift in the UV power over the duration of the measurement. The line is a phenomenological fit to extract the blockade radius R_b, where $C_6/R_b^6 = \Omega_r$. This occurs when the oscillation frequency is halfway between Ω_r and $\sqrt{2}\Omega_r$. In all panels, the error bars show $\pm 1\sigma$ statistical error.

hyperfine-induced Förster resonances in ^{87}Sr were recently theoretically predicted [43]. A detailed characterization of the ^{171}Yb Rydberg series, as well as a detailed calculation of their interaction potentials and comparison with experiment, is left to future work.

APPENDIX D: GATE FIDELITY CALCULATIONS

In this section, we estimate the two-qubit gate fidelity from the experimental data, incorporating the effects of Rydberg state leakage and SPAM errors. Our approach follows Ref. [7] closely.

We wish to estimate the Bell state fidelity using the expression [37]

$$\mathcal{F} = \frac{1}{2}(p_{00} + p_{11} + \mathcal{C}), \tag{D1}$$

where p_{00} (p_{11}) is the population in state $|00\rangle$ ($|11\rangle$) and $\mathcal{C}$ is the contrast obtained from the parity oscillation measurement [Fig. 4(e)].

In the experiment, population can also reside outside of the computational states $\{|0\rangle, |1\rangle\}$, for example, by leaking to $|r\rangle$. Noncomputational states do not fluoresce during the state readout and, therefore, are misidentified as being in $|1\rangle$ (Sec. III). This leads to an overestimation of p_{11}. We can explicitly write the probability of the measurement outcomes A_{ij} in terms of the atomic state populations as

$$\begin{aligned} A_{00} &= p_{00}, \\ A_{01} &= p_{01} + p_{0r}, \\ A_{10} &= p_{10} + p_{r0}, \\ A_{11} &= p_{11} + p_{1r} + p_{r1} + p_{rr}. \end{aligned} \tag{D2}$$

Here, the subscript r represents any state outside of the computational basis.

To obtain a better estimate of the populations p_{ij}, we repeat the experiment without the blowout. In this case, both $|0\rangle$ and $|1\rangle$ are bright, while everything outside the computational basis is dark. The probability of each outcome, B_{ij}, can be written in terms of p_{ij} as

$$\begin{aligned} B_{bb} &= p_{00} + p_{01} + p_{10} + p_{11}, \\ B_{bd} &= p_{0r} + p_{1r}, \\ B_{db} &= p_{r0} + p_{r1}, \\ B_{dd} &= p_{rr}. \end{aligned} \tag{D3}$$

Combining these equations, we derive expressions for p_{ij}:

$$\begin{aligned} p_{00} &= A_{00}, \\ p_{01} &= A_{01} - B_{bd} + p_{1r}, \\ p_{10} &= A_{10} - B_{db} + p_{r1}, \\ p_{11} &= A_{11} - B_{dd} - B_{bd} - B_{db} + p_{0r} + p_{r0}. \end{aligned}$$

Since probabilities are non-negative, we can obtain lower bounds for p_{ij}:

$$p_{00} = A_{00}, \tag{D4}$$

$$p_{01} \geq A_{01} - B_{bd}, \tag{D5}$$

$$p_{10} \geq A_{10} - B_{db}, \tag{D6}$$

$$p_{11} \geq A_{11} - (1 - B_{bb}). \tag{D7}$$

Experimental measurements of A_{ij} and B_{ij} after preparing the Bell state are presented in Table I. The contrast of parity oscillation is $\mathcal{C} = 0.79(3)$.

TABLE I. Experimentally measured A_{ij} and B_{ij} in Eqs. (D2) and (D3).

A_{00}	0.41(2)	B_{bb}	0.903(13)
A_{01}	0.046(8)	B_{bd}	0.044(9)
A_{10}	0.047(8)	B_{db}	0.053(10)
A_{11}	0.50(2)	B_{dd}	<0.01

TABLE II. Fidelity of qubit operations.

Spin initialization	99.8(6)%
Imaging fidelity and survival	98.8(3)%
Spin readout	97.2(4)%
Single-qubit gates (RB)	99.959(6)%
CZ gate	83(2)%

The raw Bell state fidelity computed from the A_{ij} is

$$\mathcal{F}_{\text{raw}} = \frac{1}{2}(A_{00} + A_{11} + \mathcal{C}) = 85(2)\%. \tag{D8}$$

Equation (D7) yields a lower bound for $p_{11} \geq 0.40(2)$, while $p_{00} = A_{00}$ and $\mathcal{C}$ remain unchanged. This gives rise to a lower bound on the true Bell state fidelity of

$$\mathcal{F} = \frac{1}{2}(p_{00} + p_{11} + \mathcal{C}) \geq 80(2)\%.$$

This is lower than $\mathcal{F}_{\text{raw}}$, because it accounts for leakage out of the computational space, which has a greater impact on the fidelity than population in the wrong computational state.

Additionally, we wish to estimate the impact SPAM errors. In our experiment, the main source of SPAM error is atom loss during the initialization and measurement phases.

If one of the two atoms is lost before the gate, the final state of the remaining atom (for the ideal circuit) is $|\psi\rangle = (|0\rangle + e^{i\phi}|1\rangle)/\sqrt{2}$, which yields the measurement result 11 or 10/01 with equal probability. These events do not contribute to the parity oscillation, since the oscillation period is different from the Bell state.

Meanwhile, if an atom is lost after the gate, the remaining atom can be described by the mixed state $\rho = \mathbb{1}/2$. This gives the same measurement results as if the atom was lost before the gate and does not oscillate at all during the parity oscillation measurement.

Therefore, atom loss before and after the gate contribute in the same way to the measurement results. Given an overall loss rate of ϵ per atom, we can correct p_{00} and $\mathcal{C}$ by multiplying by a factor of $(1-\epsilon)^{-2}$:

$$p_{00}^c = \frac{p_{00}}{(1-\epsilon)^2}, \tag{D9}$$

$$\mathcal{C}^c = \frac{\mathcal{C}}{(1-\epsilon)^2}. \tag{D10}$$

In the case of p_{11}, we must consider that losing one of the atoms results in the outcome 11 with probability 1/2, while losing both the atoms results in 11 with probability 1. Thus, we can write

$$\begin{aligned} p_{11} &= p_{11}^c(1-\epsilon)^2 + 0.5 \times \epsilon(1-\epsilon) + 0.5 \times (1-\epsilon)\epsilon + \epsilon^2 \\ &= p_{11}^c(1-\epsilon)^2 + \epsilon. \end{aligned}$$

This gives rise to the corrected population in $|11\rangle$:

$$p_{11}^c = \frac{p_{11} - \epsilon}{(1-\epsilon)^2}. \tag{D11}$$

Using independent experiments, we conservatively estimate the atom loss probability to be $\epsilon \geq 2.4(6)\%$. Utilizing Eqs. (D9)–(D11), we are able to put a lower bound on the Bell state fidelity after SPAM correction:

$$\mathcal{F}^c = \frac{1}{2}(p_{00}^c + p_{11}^c + \mathcal{C}^c) \geq 83(2)\%. \tag{D12}$$

In Sec. V, we demonstrate that the gate can also be suppressed by the 369 nm laser. Therefore, the final state should be $|00\rangle$ [see Fig. 5(a)]. In the experiment, we measure a raw fidelity of $\mathcal{F}_I = p_{00} = 84(2)\%$. On the day that these measurements were performed, the atom survival rate after imaging and rearrangement was atypically bad, relying on an out-of-date imaging calibration dataset, and we independently measured the atom loss $\epsilon = 4.6(5)\%$. From this measurement, we correct the fidelity $\mathcal{F}_I^c = p_{00}^c = 93(2)\%$ using Eq. (D9).

APPENDIX E: SUMMARY OF MEASURED OPERATION FIDELITIES

In Table II, we summarize the fidelity of the qubit operations discussed in the main text.

[1] M. Saffman, *Quantum Computing with Atomic Qubits and Rydberg Interactions: Progress and Challenges*, J. Phys. B **49**, 202001 (2016).

[2] A. Browaeys and T. Lahaye, *Many-Body Physics with Individually Controlled Rydberg Atoms*, Nat. Phys. **16**, 132 (2020).

[3] S. Ebadi, T. T. Wang, H. Levine, A. Keesling, G. Semeghini, A. Omran, D. Bluvstein, R. Samajdar, H. Pichler, W. W. Ho, S. Choi, S. Sachdev, M. Greiner, V. Vuletić, and M. D. Lukin, *Quantum Phases of Matter on a 256-Atom Programmable Quantum Simulator*, Nature (London) **595**, 227 (2021).

[4] P. Scholl, M. Schuler, H. J. Williams, A. A. Eberharter, D. Barredo, K.-N. Schymik, V. Lienhard, L.-P. Henry, T. C. Lang, T. Lahaye, A. M. Läuchli, and A. Browaeys, *Quantum Simulation of 2D Antiferromagnets with Hundreds of Rydberg Atoms*, Nature (London) **595**, 233 (2021).

[5] G. Semeghini, H. Levine, A. Keesling, S. Ebadi, T. T. Wang, D. Bluvstein, R. Verresen, H. Pichler, M. Kalinowski, R. Samajdar, A. Omran, S. Sachdev, A. Vishwanath, M. Greiner, V. Vuletić, and M. D. Lukin, *Probing Topological Spin Liquids on a Programmable Quantum Simulator*, Science **374**, 1242 (2021).

[6] T. M. Graham, M. Kwon, B. Grinkemeyer, Z. Marra, X. Jiang, M. T. Lichtman, Y. Sun, M. Ebert, and M. Saffman, *Rydberg-Mediated Entanglement in a Two-Dimensional Neutral Atom Qubit Array*, Phys. Rev. Lett. **123**, 230501 (2019).

[7] H. Levine, A. Keesling, G. Semeghini, A. Omran, T. T. Wang, S. Ebadi, H. Bernien, M. Greiner, V. Vuletić, H. Pichler, and M. D. Lukin, *Parallel Implementation of High-Fidelity Multiqubit Gates with Neutral Atoms*, Phys. Rev. Lett. **123**, 170503 (2019).

[8] A. Omran, H. Levine, A. Keesling, G. Semeghini, T. T. Wang, S. Ebadi, H. Bernien, A. S. Zibrov, H. Pichler, S. Choi, J. Cui, M. Rossignolo, P. Rembold, S. Montangero, T. Calarco, M. Endres, M. Greiner, V. Vuletić, and M. D. Lukin, *Generation and Manipulation of Schrödinger Cat States in Rydberg Atom Arrays*, Science **365**, 570 (2019).

[9] J. Choi, A. L. Shaw, I. S. Madjarov, X. Xie, J. P. Covey, J. S. Cotler, D. K. Mark, H.-Y. Huang, A. Kale, H. Pichler, F. G. S. L. Brandão, S. Choi, and M. Endres, *Emergent Randomness and Benchmarking from Many-Body Quantum Chaos*, arXiv:2103.03535.

[10] A. Cooper, J. P. Covey, I. S. Madjarov, S. G. Porsev, M. S. Safronova, and M. Endres, *Alkaline-Earth Atoms in Optical Tweezers*, Phys. Rev. X **8**, 041055 (2018).

[11] M. A. Norcia, A. W. Young, and A. M. Kaufman, *Microscopic Control and Detection of Ultracold Strontium in Optical-Tweezer Arrays*, Phys. Rev. X **8**, 041054 (2018).

[12] K. Barnes, P. Battaglino, B. J. Bloom, K. Cassella, R. Coxe, N. Crisosto, J. P. King, S. S. Kondov, K. Kotru, S. C. Larsen, J. Lauigan, B. J. Lester, M. McDonald, E. Megidish, S. Narayanaswami, C. Nishiguchi, R. Notermans, L. S. Peng, A. Ryou, T.-Y. Wu, and M. Yarwood, *Assembly and Coherent Control of a Register of Nuclear Spin Qubits*, arXiv:2108.04790.

[13] S. Saskin, J. T. Wilson, B. Grinkemeyer, and J. D. Thompson, *Narrow-Line Cooling and Imaging of Ytterbium Atoms in an Optical Tweezer Array*, Phys. Rev. Lett. **122**, 143002 (2019).

[14] J. T. Wilson, S. Saskin, Y. Meng, S. Ma, R. Dilip, A. P. Burgers, and J. D. Thompson, *Trapping Alkaline Earth Rydberg Atoms Optical Tweezer Arrays*, Phys. Rev. Lett. **128**, 033201 (2022).

[15] I. S. Madjarov, J. P. Covey, A. L. Shaw, J. Choi, A. Kale, A. Cooper, H. Pichler, V. Schkolnik, J. R. Williams, and M. Endres, *High-Fidelity Entanglement and Detection of Alkaline-Earth Rydberg Atoms*, Nat. Phys. **16**, 857 (2020).

[16] A. P. Burgers, S. Ma, S. Saskin, J. Wilson, M. A. Alarcón, C. H. Greene, and J. D. Thompson, *Controlling Rydberg Excitations Using Ion Core Transitions in Alkaline Earth Atom Tweezer Arrays*, arXiv:2110.06902 [PRX Quantum (to be published)].

[17] K.-L. Pham, T. Gallagher, P. Pillet, S. Lepoutre, and P. Cheinet, *A Coherent Light Shift on Alkaline-Earth Rydberg Atoms from Isolated Core Excitation without Autoionization*, arXiv:2111.00982 [PRX Quantum (to be published)].

[18] M. A. Norcia, A. W. Young, W. J. Eckner, E. Oelker, and J. Ye, and A. M. Kaufman, *Seconds-Scale Coherence on an Optical Clock Transition in a Tweezer Array*, Science **366**, 93 (2019).

[19] I. S. Madjarov, A. Cooper, A. L. Shaw, J. P. Covey, V. Schkolnik, T. H. Yoon, J. R. Williams, and M. Endres, *An Atomic-Array Optical Clock with Single-Atom Readout*, Phys. Rev. X **9**, 041052 (2019).

[20] N. Schine, A. W. Young, W. J. Eckner, M. J. Martin, and A. M. Kaufman, *Long-Lived Bell States in an Array of Optical Clock Qubits*, arXiv:2111.14653.

[21] S. Kuhr, W. Alt, D. Schrader, I. Dotsenko, Y. Miroshnychenko, A. Rauschenbeutel, and D. Meschede, *Analysis of Dephasing Mechanisms in a Standing-Wave Dipole Trap*, Phys. Rev. A **72**, 023406 (2005).

[22] S. Dörscher, R. Schwarz, A. Al-Masoudi, S. Falke, U. Sterr, and C. Lisdat, *Lattice-Induced Photon Scattering in an Optical Lattice Clock*, Phys. Rev. A **97**, 063419 (2018).

[23] A. Noguchi, Y. Eto, M. Ueda, and M. Kozuma, *Quantum-State Tomography of a Single Nuclear Spin Qubit of an Optically Manipulated Ytterbium Atom*, Phys. Rev. A **84**, 030301(R) (2011).

[24] J. Beugnon, C. Tuchendler, H. Marion, A. Gaëtan, Y. Miroshnychenko, Y. R. P. Sortais, A. M. Lance, M. P. A. Jones, G. Messin, A. Browaeys, and P. Grangier, *Two-Dimensional Transport and Transfer of a Single Atomic Qubit in Optical Tweezers*, Nat. Phys. **3**, 696 (2007).

[25] T. Xia, M. Lichtman, K. Maller, A. W. Carr, M. J. Piotrowicz, L. Isenhower, and M. Saffman, *Randomized Benchmarking of Single-Qubit Gates in a 2D Array of Neutral-Atom Qubits*, Phys. Rev. Lett. **114**, 100503 (2015).

[26] R. Guo, X. He, C. Sheng, J. Yang, P. Xu, K. Wang, J. Zhong, M. Liu, J. Wang, and M. Zhan, *Balanced Coherence Times of Atomic Qubits of Different Species in a Dual* 3×3 *Magic-Intensity Optical Dipole Trap Array*, Phys. Rev. Lett. **124**, 153201 (2020).

[27] N. D. Lemke, A. D. Ludlow, Z. W. Barber, T. M. Fortier, S. A. Diddams, Y. Jiang, S. R. Jefferts, T. P. Heavner, T. E. Parker, and C. W. Oates, *Spin-*$1/2$ *Optical Lattice Clock*, Phys. Rev. Lett. **103**, 063001 (2009).

[28] R. Yamamoto, J. Kobayashi, T. Kuno, K. Kato, and Y. Takahashi, *An Ytterbium Quantum Gas Microscope with Narrow-Line Laser Cooling*, New J. Phys. **18**, 023016 (2016).

[29] S. G. Porsev, Y. G. Rakhlina, and M. G. Kozlov, *Electric-Dipole Amplitudes, Lifetimes, and Polarizabilities of the Low-Lying Levels of Atomic Ytterbium*, Phys. Rev. A **60**, 2781 (1999).

[30] Z. W. Barber, J. E. Stalnaker, N. D. Lemke, N. Poli, C. W. Oates, T. M. Fortier, S. A. Diddams, L. Hollberg, C. W. Hoyt, A. V. Taichenachev, and V. I. Yudin, *Optical Lattice Induced Light Shifts in an Yb Atomic Clock*, Phys. Rev. Lett. **100**, 103002 (2008).

[31] G. Lochead, D. Boddy, D. P. Sadler, C. S. Adams, and M. P. A. Jones, *Number-Resolved Imaging of Excited-State Atoms Using a Scanning Autoionization Microscope*, Phys. Rev. A **87**, 053409 (2013).

[32] E. Nielsen, K. Rudinger, T. Proctor, A. Russo, K. Young, and R. Blume-Kohout, *Probing Quantum Processor Performance with pyGSTi*, Quantum Sci. Technol. **5**, 044002 (2020).

[33] M. D. Lukin, M. Fleischhauer, R. Cote, L. M. Duan, D. Jaksch, J. I. Cirac, and P. Zoller, *Dipole Blockade and Quantum Information Processing in Mesoscopic Atomic Ensembles*, Phys. Rev. Lett. **87**, 037901 (2001).

[34] L. Isenhower, E. Urban, X. L. Zhang, A. T. Gill, T. Henage, T. A. Johnson, T. G. Walker, and M. Saffman, *Demonstration of a Neutral Atom Controlled-Not Quantum Gate*, Phys. Rev. Lett. **104**, 010503 (2010).

[35] Y. Y. Jau, A. M. Hankin, T. Keating, I. H. Deutsch, and G. W. Biedermann, *Entangling Atomic Spins with a Rydberg-Dressed Spin-Flip Blockade*, Nat. Phys. **12**, 71 (2016).

[36] T. Wilk, A. Gaëtan, C. Evellin, J. Wolters, Y. Miroshnychenko, P. Grangier, and A. Browaeys, *Entanglement of Two Individual Neutral Atoms Using Rydberg Blockade*, Phys. Rev. Lett. **104**, 010502 (2010).

[37] C. A. Sackett, D. Kielpinski, B. E. King, C. Langer, V. Meyer, C. J. Myatt, M. Rowe, Q. A. Turchette, W. M. Itano, D. J. Wineland, and C. Monroe, *Experimental Entanglement of Four Particles*, Nature (London) **404**, 256 (2000).

[38] S. de Léséleuc, D. Barredo, V. Lienhard, A. Browaeys, and T. Lahaye, *Analysis of Imperfections in the Coherent Optical Excitation of Single Atoms to Rydberg States*, Phys. Rev. A **97**, 053803 (2018).

[39] J. Yang, X. He, R. Guo, P. Xu, K. Wang, C. Sheng, M. Liu, J. Wang, A. Derevianko, and M. Zhan, *Coherence Preservation of a Single Neutral Atom Qubit Transferred between Magic-Intensity Optical Traps*, Phys. Rev. Lett. **117**, 123201 (2016).

[40] H. Levine, D. Bluvstein, A. Keesling, T. T. Wang, S. Ebadi, G. Semeghini, A. Omran, M. Greiner, V. Vuletić, and M. D. Lukin, *Dispersive Optical Systems for Scalable Raman Driving of Hyperfine Qubits*, Phys. Rev. A **105**, 032618 (2022).

[41] H. Levine, A. Keesling, A. Omran, H. Bernien, S. Schwartz, A. S. Zibrov, M. Endres, M. Greiner, V. Vuletić, and M. D. Lukin, *High-Fidelity Control and Entanglement of Rydberg-Atom Qubits*, Phys. Rev. Lett. **121**, 123603 (2018).

[42] C. L. Vaillant, M. P. A. Jones, and R. M. Potvliege, *Long-Range Rydberg–Rydberg Interactions in Calcium, Strontium and Ytterbium*, J. Phys. B **45**, 135004 (2012).

[43] F. Robicheaux, *Calculations of Long Range Interactions for* ^{87}Sr *Rydberg States*, J. Phys. B **52**, 244001 (2019).

[44] J. P. Covey, I. S. Madjarov, A. Cooper, and M. Endres, *2000-Times Repeated Imaging of Strontium Atoms in Clock-Magic Tweezer Arrays*, Phys. Rev. Lett. **122**, 173201 (2019).

[45] L. I. R. Gil, R. Mukherjee, E. M. Bridge, M. P. A. Jones, and T. Pohl, *Spin Squeezing in a Rydberg Lattice Clock*, Phys. Rev. Lett. **112**, 103601 (2014).

[46] R. Kaubruegger, P. Silvi, C. Kokail, R. van Bijnen, A. M. Rey, J. Ye, A. M. Kaufman, and P. Zoller, *Variational Spin-Squeezing Algorithms on Programmable Quantum Sensors*, Phys. Rev. Lett. **123**, 260505 (2019).

[47] A. Jenkins, J. W. Lis, A. Senoo, W. F. McGrew, and A. M. Kaufman, preceding paper, *Ytterbium Nuclear-Spin Qubits in an Optical Tweezer Array*, Phys. Rev. X **12**, 021027 (2022).

[48] B. Arora, M. S. Safronova, and C. W. Clark, *Magic Wavelengths for the* $np - ns$ *Transitions in Alkali-Metal Atoms*, Phys. Rev. A **76**, 052509 (2007).

[49] P. Liao, R. Freeman, R. Panock, and L. Humphrey, *Hyperfine-Induced Singlet-Triplet Mixing in 3He*, Opt. Commun. **34**, 195 (1980).

[50] R. Beigang, E. Matthias, and A. Timmermann, *Influence of Singlet-Triplet Mixing on the Hyperfine Structure of* $5snd$ *Rydberg States in* ^{87}Sr, Phys. Rev. Lett. **47**, 326 (1981).

[51] M. Aymar, *Rydberg Series of Alkaline-Earth Atoms Ca through Ba. The Interplay of Laser Spectroscopy and Multichannel Quantum Defect Analysis*, Phys. Rep. **110**, 163 (1984).

[52] K. Singer, J. Stanojevic, M. Weidemüller, and R. Côté, *Long-Range Interactions between Alkali Rydberg Atom Pairs Correlated to the ns–ns, np–np and nd–nd Asymptotes*, J. Phys. B **38**, S295 (2005).

[53] M. Saffman, T. G. Walker, and K. Mølmer, *Quantum Information with Rydberg Atoms*, Rev. Mod. Phys. **82**, 2313 (2010).